ENTREGABLE E7

Pruebas de usabilidad

Informe del test de planificación quirúrgica

Programa	Valorización y transferencia de resultados de investigación a las empresas
Línea de Actuación	L1. Valorización, transferencia y explotación por las empresas de resultados de I+D
Entidad Beneficiaria	UNIVERSIDAD MIGUEL HERNANDEZ DE ELCHE
NIF	Q5350015C
Título del Proyecto	Sistema no invasivo para la caracterización bioquímica, detección de componentes, y reconstrucción biomédica 3D de tejidos biológicos
Número de Expediente	INNVA1/2020/49

Tabla de contenido

Introducción

De acuerdo a la memoria, se realizó una experimentación para tener una prueba de usabilidad del sistema desarrollado en un escenario diferente de la detección de tejido en mama. Para ello se había seleccionado un escenario de cirugía de precisión, en la que el sistema desarrollado tenía que ser capaz de obtener imágenes intraoperatorias de la herramienta quirúrgica y del tumor objetivo donde debía moverse la herramienta. Para esta ocasión, la herramienta quirúrgica se colocó en el extremo de un robot.

Experimental setup

Once the system was implemented and calibrated, its performance as cranial surgery navigation tool was assessed. The targeted application consists in detecting the position of the surgical tool within the cranial area, so that the surgical team is provided with proper guidance and assistance. In order to emulate such a scenario, a setup imitating an operating room for cranial surgical interventions with robotic tools was prepared, as shown in Figure 8. As shown, a structure was designed to hold the antenna system, allowing to house the 3-D-printed cranium in the exact center. Ad hoc connection of the antennas to the VNA and the computer was installed, as explained in the prior sections, to allow the proper running of the microwave image system. Finally, a UR5 robotic arm was used to emulate the surgeon's moves. The robotic arm was configured to hold the clinical tool, which is intended to navigate towards the critical area within the cranium.

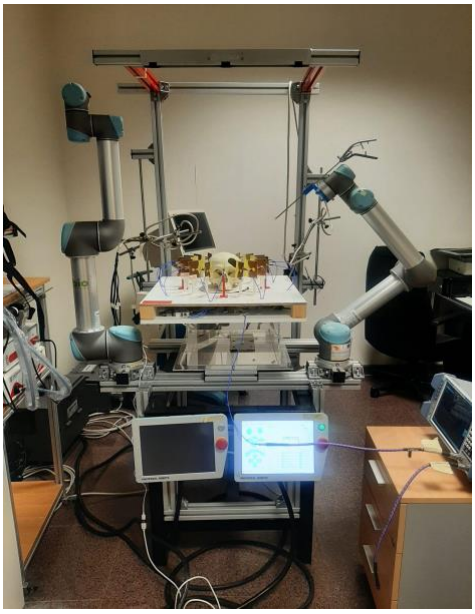

Figure 8. Experimental setup.

For the experimental validation an accurate and detailed 3-D-printed model for the cranium was used (horizontal section dimensions 128×170 mm2), which had a hole on the left-side forehead to enable the entrance of the surgical tool, thereby allowing us to simulate intracranial surgery. A piece of plastic filled with water was used to imitate a tumor, which was placed inside the cranium, in the inner center-forehead area (Figure 9). The cranium was placed in the center of the antenna system, so that the cranium's center coincided with the center of the antennas' coordinate system, as it can be seen in the picture. With this configuration, the tumor was slightly displaced from the center of the coordinate system, being the tumor's center position at roughly (0, 26) mm coordinates considering the framework in Figure 9. The tumor had 25×25×25 mm3 dimensions.

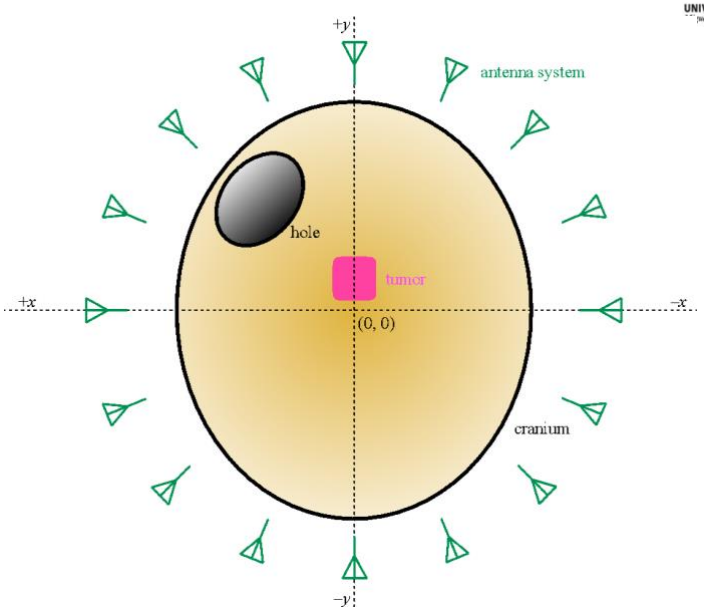

Figure 9. Schematic representation of the cranium (yellow), the hole (black), the tumor (pink), the antennas (green) and the coordinate system.

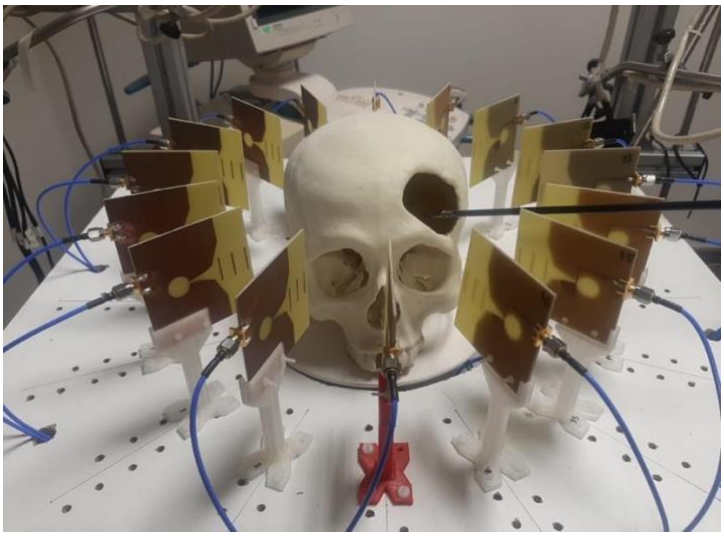

Figure 10. Experimental setup with the tool entering the cranium within the antenna system.

The navigation sequence for the experimental validation consisted in the surgical tool being approached to the tumor, throughout the cranium's hole, following a spatially-diagonal straight line (also including approach in z coordinate, which is not considered in the 2-D images provided by the microwave image system) at the same time that the microwave image system was tracking the tool position. The tool path started at a position sufficiently far from the tumor (more than 150 mm away), and it was planned to finish as close as possible to the tumor's center, thus resembling the trajectory followed during an actual intervention. Although the tool may be handled by the surgeon in real operations, the robotic arm was used to hold it during this experiment so that the trajectory and navigation sequence could be accurately controlled, and reference coordinates throughout the trajectory could be obtained in a reliable manner. A picture of the tool entering the cranium and the antenna system can be seen in Figure 10.

Image acquisition

Before starting the experiment, a measurement only having the antennas, with nothing inside the system (empty measurement) was made. This empty measurement was used as reference and calibration measurement throughout the whole experiment, and all the rest of images presented in this work included the subtraction of this empty measurement. Then, two initial measurements were made with the microwave image system for the proposed setup: one only having the cranium (no tumor, no tool), and another one having the cranium and the tumor (no tool) in the right positions. During the navigation sequence, 8 measurements were made with the microwave image system at 8 different moments, so that the 8 corresponding images could be assessed. Parallelly to each of them, the coordinates of the robotic arm at each moment were saved, which were later transformed to tool's final-end coordinates for reference. Within these 8 positions, hereinafter referred to as pi, where $1 \leq i \leq 8$, p1 and p2 had the tool's final end out of the antenna system space, p3 and p4 had it inside the antenna system space but out of the cranium, p5 had it approximately in the cranium boundary (entering the hole), p6 and p7 had it inside the cranium and gradually approaching the tumor, and p8 had it inside the cranium and well-nigh touching the tumor boundary. Finally, the 10 resulting measurements (2 initial ones + 8 during the tool's navigation) were processed with both DAS and DMAS algorithms.

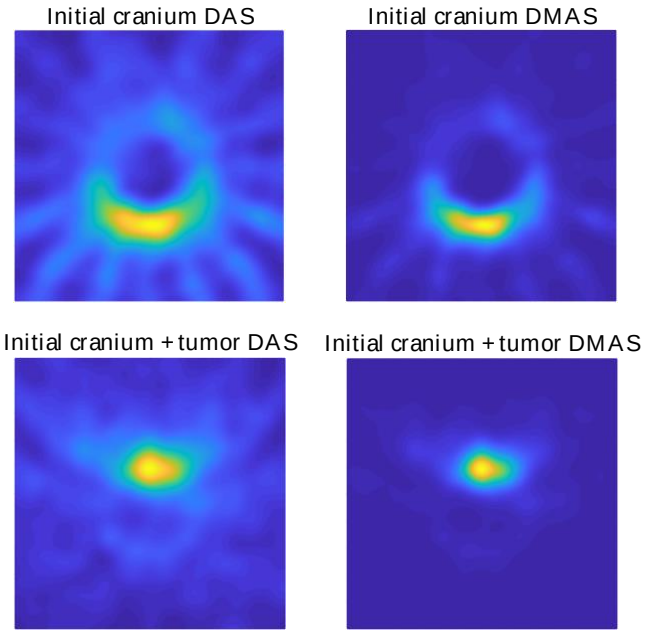

Figure 11. Initial images with DAS and DMAS algorithms.

The resulting images for both DAS and DMAS algorithms as for the 2 initial measurements are shown in Figure 11, whereas the corresponding images for a selection of some of the 8 navigation measurements can be seen in Figure 12 (positions 1 and 2 are not shown since the tool was out of the antenna system area). The images in Figure 12 show the evolution of the tool's final-end position during the navigation experiment, although some other reflections are detected due to the long-shaped tool's body. Considering a long enough tool (which is the most usual case in these operations), these reflections are approximately constant for two consecutive images or positions (provided that a low or moderate differential movement was made), being the new information only

related to the position change. Therefore, aiming at a better detection of the tool's final-end position for navigation purposes, the images were further processed by subtracting the previous image from the current one, so that only the tool's displacement information was left, and the new position can be easily tracked. The resulting images for both algorithms are shown in Figure 13, again excluding positions 1 and 2 for the same reason.

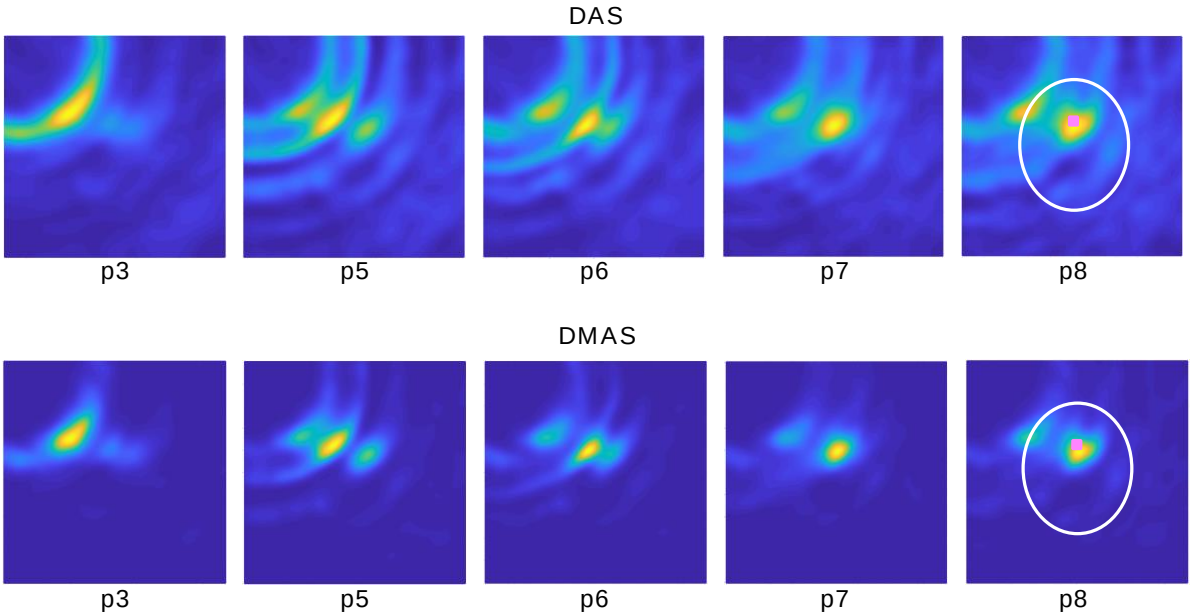

Figure 12. Navigation images for a selection of the positions obtained with DAS and DMAS algorithms. The position and shape of the cranium (white) and tumor (pink) is depicted in the last image for reference.

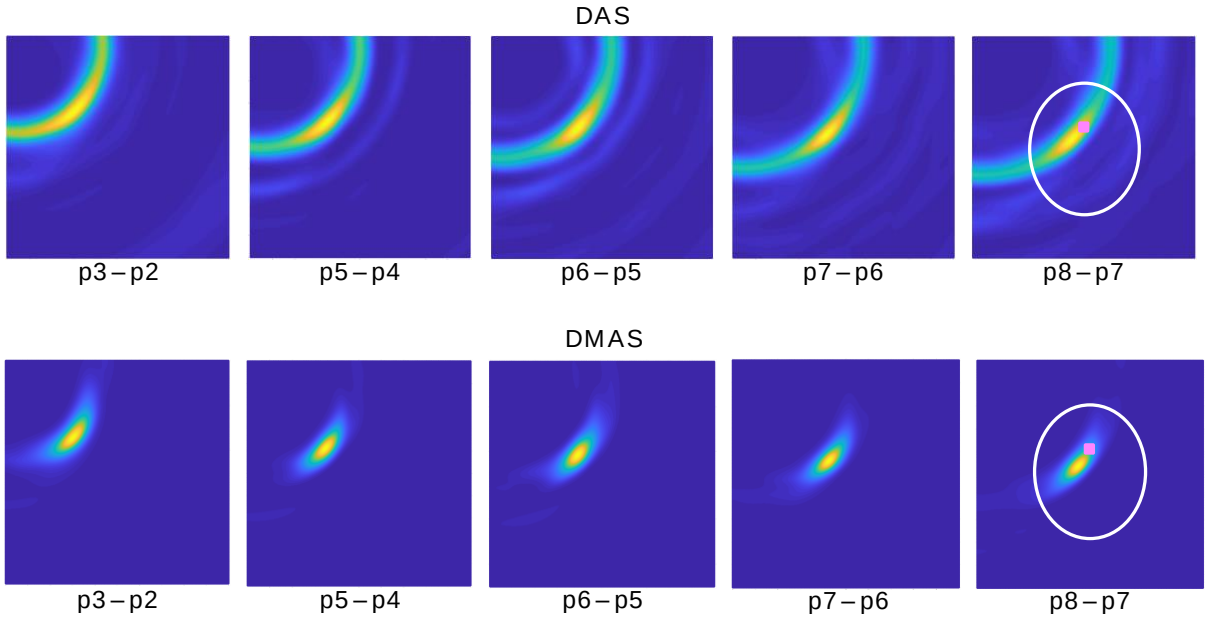

Figure 13. Differential navigation images for a selection of the positions obtained with DAS and DMAS algorithms. The position and shape of the cranium (white) and tumor (pink) is depicted in the last image for reference.

Data extraction and results

The images in Figure 13 show a clear evolution of the tool's final-end position throughout the trajectory. These images are therefore suitable to provide for the targeted navigation track. To provide for navigation assistance and guidance accurate capabilities, the exact coordinates of the tool's position must be detected. To that end, each image in Figure 13 was binarized with 0.8 threshold, which means that a new binary black-and-white associated image was created in which the pixels having luminance < 0.8 in the original image were set to black, otherwise to white. An example of this process for "p5 – p4" images for both algorithms is shown in Figure 14. As it can be seen, the resulting images are more convenient for properties processing and detection. Each binarized image was then analyzed and the coordinates of the centroid of the remaining white region were computed. As seen in Figure 13, the high-luminance regions correspond to the tool's final-end positions, and therefore these centroids' coordinates were associated to the real tool's final-end coordinates.

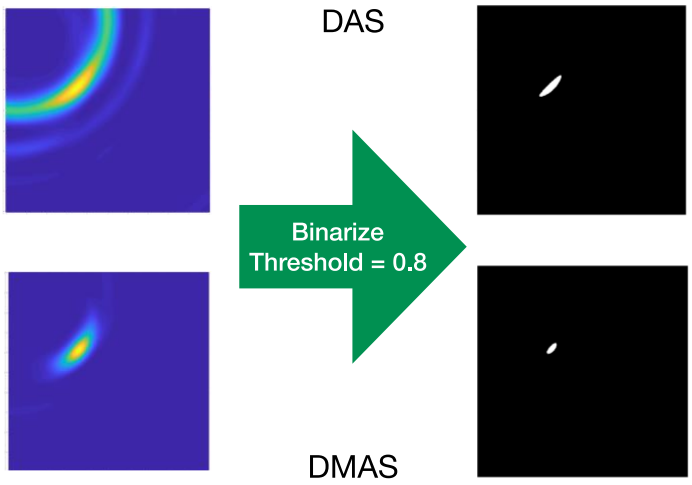

Figure 14. Example of binarization process for "p5 – p4" images.

The binarized images had 1300 × 1301 dimensions. The computed centroids were defined within an image-based coordinate system, having the origin in the top-left corner. In order to be able to compare with the reference coordinates of the tool's final end, which were obtained through the robotic arm positions, considering the common coordinate system centered in the antenna system (and in the cranium as well), the equivalence of pixels to physical distance was required. These data were obtained thanks to the real cranium dimensions and its pixel-based dimensions computed from the initial cranium images (see Figure 11 top). The equivalence was thereby found to be 1 column pixel = 0.1922 mm; 1 row pixel = 0.2255 mm. With these data, the microwave image-based detected tool's final-end coordinates were obtained. A scheme of the coordinate detection process is depicted in Figure 15.

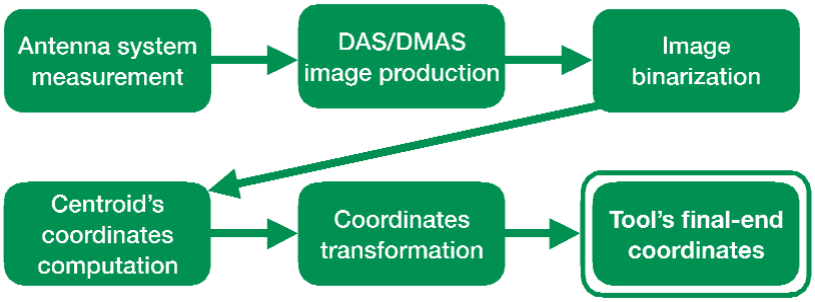

Figure 15. Scheme of the coordinate detection process.

The results for the detection of the tool's final-end coordinates are shown in Table 1, which gathers the detected coordinates both with DAS and DMAS algorithms when the differential images (Figure 13) are considered, and compares them to the reference coordinates obtained from the robotic arm at each position. Position p1 is not considered since there was no prior position to perform the image subtraction and the tool was considerably far from the antenna system. The evolution of the detected coordinates with both algorithms, as well as the reference coordinates from the robot, show the approaching trajectory of the tool to the tumor, from p2 to p8. Specifically, the detected coordinates in p8 for DAS and DMAS algorithms show a difference of (12.5886, -15.1963) mm and (12.3963, -15.7374) mm, respectively, with respect to the corresponding detected coordinates of the tumor's center, which are coherent with the visual observation (see Figure 16). This is also confirmed by the small error in p8 for DAS and DMAS with respect to the reference coordinates from the robot: $\Delta(p8) = (-0.8544, -0.5576)$ mm for DAS and $\Delta(p8) = (-1.3925, -0.1743)$ mm for DMAS.

Table 1. Detected tool's final-end coordinates (in mm).

Positions	**DAS**		**DMAS**		**Robot**	
	x	***y***	***x***	***y***	***x***	***y***
Tumor	-0.6342	26.1538	0.0961	26.3117	—	—
p2	80.6823	0.4284	111.0871	-13.9562	90.4000	96.2000
p3	47.4907	47.0544	47.4907	44.3263	67.0000	70.8000
p4	42.3399	37.4496	41.8595	36.3899	58.6000	61.7000
p5	36.3243	32.8501	36.1898	31.7679	45.8000	47.9000
p6	26.1574	25.5000	26.1189	24.0119	29.5000	30.2000
p7	17.7778	17.4735	17.8162	16.4589	19.6000	19.5000
p8	11.9544	10.9576	12.4925	10.5743	11.1000	10.4000

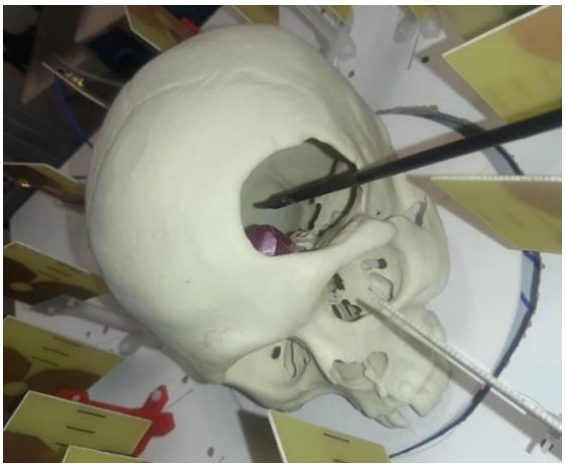

Figure 16. Tool inside the cranium at position p7.

Considering the reference coordinates from the robot, Table 2 shows an error analysis for the performance of DAS and DMAS. Position p2 has been excluded because the tool was still too far from the antenna system region. The mean error ($\underline{\Delta}$) and the standard deviation (σ) for each coordinate (x and y) are independently considered in this analysis. Also, different ranges of positions are involved, depending on the different regions where the tool navigated: p3 to p8 includes the tool travelling through the antenna system inner space, the cranium boundary and the cranium inner space, p5 to p8 includes the tool travelling through the cranium boundary and its inner space, and p6 to p8 includes only the tool travelling through the cranium inner space.

Table 2. Error analysis for both algorithms (data in mm).

Position range	DAS				DMAS			
	$\underline{\Delta x}$	$\underline{\Delta y}$	σ_x	σ_y	$\underline{\Delta x}$	$\underline{\Delta y}$	σ_x	σ_y
p3 to p8	8.2593	11.5358	8.2550	11.0136	8.2721	12.8285	8.4759	11.5053
p5 to p8	3.4465	5.3047	4.3779	6.8422	3.3456	6.2968	4.6237	7.0526
p6 to p8	1.4368	2.0563	2.1249	2.6289	1.2575	3.0183	2.4299	3.1812

Finally, the influence of the luminance threshold was analyzed. Given the agreement between the detected coordinates with both algorithms at p8 and the reference coordinates from the robot arm, this position was taken as general reference. The detected coordinates were recalculated from the saved measurements with DAS and DMAS algorithms using different luminance thresholds. For each newly recalculated pair of coordinates (associated to a certain luminance threshold), the detection error (DE) was computed as the Euclidean distance to the reference coordinates:

$$DE = \sqrt{|x_d - x_r|^2 + |y_d - y_r|^2} \quad (6)$$

where xd and yd are the detected coordinates, whilst xr and yr are the reference coordinates. The resulting evolution of the DE depending on the luminance threshold for DAS and DMAS algorithms at p8 is plotted in Figure 17.

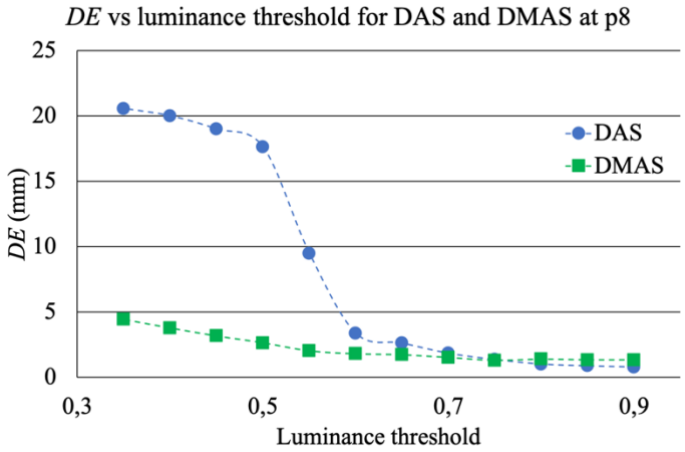

Figure 17. Evolution of *DE* depending on the luminance threshold for both algorithms.

Discussion

A microwave-based image system for cranial intraoperative tool navigation has been proposed, and its performance has been assessed. The system is composed of 16 twin Vivaldi-like antennas placed throughout a circumference with an equally-spaced pattern, surrounding the cranial surgery area, pointing to the center of the circumference. An automated switching electronic system is used to drive the antennas and make the corresponding reflection measurements. The responses of the antennas are affected by the reflections of the electromagnetic waves on the cranium shape and on strange objects, such as tumors or surgical tools. These responses are further processed to locate the desired objects, and provide for surgical tool navigation.

Two methods have been studied to process the responses of the antennas and build the medical image. These methods, viz. DAS and DMAS, consist in a spatial modelling of the surgical environment by assigning a computed intensity to each pixel of the image depending on the corresponding formulation and the time-domain response of each antenna. The following paragraphs will discuss the experimental validation and results of the proposed system using these two methods.

Figure 11 shows the capability of the proposed system to scan the cranium and detect the tumor within the experimental setup considered here. Both algorithms show acceptable detection capabilities in this regard. Considering the images in which only the cranium is involved (Figure 11 top), DAS algorithm provides brighter images, which allow us to see a higher level of details. This should be analyzed with caution, because it also implies the apparition of spurious details, such as the reflected beams captured by each antenna, which do not correspond to any physical object in the scenario. That being said, as long as the spurious information is static and previously known (such as these beams, directly related to the position of each antenna), it could be easily eliminated. DMAS algorithm, however, provides a cleaner image, almost with no spurious details, but with a more poorly defined cranium. Conversely, when the tumor is involved (Figure 11 bottom), DMAS seems to show better detection capabilities, providing a clearer, more defined location of the tumor. In this case the high-intensity reflections by the tumor material (in comparison to those by the cranium material) hinder the detection of the cranium shape in both methods, being it less visible (but detectable) for DAS algorithm, and almost invisible for DMAS algorithm. Considering these pictures, it seems that both algorithms show strengths and weaknesses for different aspects, and therefore a detailed analysis for both of them is worthy. Ostensibly, DAS

image can be more suitable for calibration tasks, for example, such as taking reference measurements of the cranium's dimensions, and also for detection and tracking of events within the cranium area, which is better resolved with this algorithm, whereas DMAS seems to show better performance as for accurate location of strange objects within the image framework, although losing information related to the cranium shape.

In the experimental results for the navigation task shown in Figure 12 it can be seen how the long shape of the tool hinders the clear and direct identification of the tool's final-end position, especially for the last positions (the tool entering the cranium, longer tool's body portion within the image). Indeed, the long-shaped tool yields the detection of many reflections throughout the tool's body by different antennas, depending on their position. This information could be useful for further processing the images in the final system, so that the full shape of the tool can be depicted in the image shown in the user-oriented graphic interface. However, for the pursued navigation assistance, considering the binarization process proposed here, this phenomenon leads to the apparition in the binarized images of several areas with several associated centroids, and the detection of the current position of the tool becomes complicated. In addition, other objects different from the tool could be detected, leading to the definition of false positions for the tool. For example, it can be seen that the tumor is detected in positions p1 and p2 with both methods, since the tool had not yet arrived to the detection area at those moments. Therefore, for navigations purposes, we propose the differential method in which the prior image is subtracted to the current one, as shown in Figure 13, so that the undesired, unmoved details are eliminated and only the information related to the tool's trajectory evolution is tracked.

Figure 13 shows the images obtained with the differential method for navigation purposes, for both algorithms. Here the information obtained from each image is only related to the tool's trajectory, i. e., the difference in the tool's final-end position between the last measurement and the current one. These images provide a clear view of the trajectory followed by the tool, starting out of the measurement area and following a straight line towards approximately the tumor's position. This approximation can be seen by observation of the images "p8 – p7" in Figure 13 and the bottom images in Figure 11. The proposed process, including the binarization of the resulting image and the computation of the centroid in the high-luminance region, allows for the detection of the tool's final-end coordinates in the current position, thereby tracking the tool's navigation. The results for this position detection process again confirm the approach of the tool to the tumor's location, as it can be seen in Table 1. Considering these results, it should be noted that: 1) tumor's position coordinates refer to the exact tumor's center, which cannot be physically reached by the tool in the proposed setup due to the physical dimensions of the solid object emulating the tumor; and 2) the tool in position p2 was out of the measurement range, and no information can be obtained from this position.

The comparison between the detected positions with both algorithms and the reference positions obtained from the robot's coordinates (Tables 1 and 2) shows a good agreement, and it therefore confirms the potential of the proposed system for intraoperative navigation imaging. The detected positions and the error analysis yield similar results for both algorithms. The error analysis results show smaller errors and standard deviations for both algorithms for the innermost region. This is coherent with the detected positions, in which the closer the tool to the tumor's position, the smaller the difference between the detected position and the reference one. Being the tumor (and the innermost region) close to the center of coordinates, this means that the error becomes smaller as the detected positions approach the center, which is logical given the radial configuration for the antenna system. As a consequence, the highest accuracy will be achieved for the innermost positions of the tool, located within the cranial area,

meaning that the system is optimized for higher accuracy and resolution in the most interesting region for cranial surgery. In this regard, the system shows a mean error of roughly 1.26 mm in the best case and 3.02 mm in the worst case for the interesting region with respect to the reference coordinates. Considering the cranium total dimensions, this means errors between 0.98 % (best case) and 1.78 % (worst case). It should be noted that, for magnetic-based tracking systems, mean detection errors of ~0.5 ± 0.5 mm have been reported [24], which can raise up to 27 mm due to interference of metallic object [8]. For optical tracking, mean errors of 0.24 ± 1.05 mm have been reported, which can raise up to 1.65 ± 5.07 mm when some cameras are occluded [7].

Figure 13 also shows that, after the previous image subtraction, DAS algorithm does not provide a graphical view of the tool's final-end position in as a clear and well-defined manner as DMAS algorithm does. Notwithstanding that, in this case, given the simple shape of the tool, the results as to the position detection after the binarization and centroid computation process are quite similar for both algorithms, as shown in Table 1. That being said, the visual inspection of Figure 13 suggests that DAS algorithm is more sensible to the luminance threshold (kept constant at 0.8 throughout the whole results analysis). Indeed, lower thresholds would have resulted in a sort of half-moon-shaped white areas in the binarized images, instead of the ellipsoid-shaped ones for 0.8, as shown in Figure 14. Being the centroids computed as the mass center of the white area, a lower threshold would lead to a displacement of the finally detected position, thus yielding to a greater error in the detection. Figure 13 confirms that this phenomenon is considerably less noticeable for DMAS algorithm. The analysis of the detection error as a function of the luminance threshold is shown in Figure 17, which confirms this behavior. These results highlight the dependence of DAS to the luminance threshold, and allow us to conclude that DMAS is more robust to DAS to variations of this parameter. Consequently, DMAS is expected to show a more reliable performance when tools having more complex shapes are considered, or when rotations of the tool are involved.

Apart from this criterion, no further reasons have been detected to claim the outperformance of one algorithm with respect to the other one. It should be noted that the setup considered in this study inherently has a certain instrumental error as for the reference coordinates obtained from the position of the robot, due to the vibrations of the links of the robot during the movement as well as the oscillations of the tool's final end due to its long shape and the tip-based holding. Therefore, seeing the small differences in the performance of both algorithms (see Tables 1 and 2), both algorithms show acceptable performance for intraoperative tool's navigation tracking, and we cannot point to any algorithm to be the most advantageous as for the detection accuracy for the experimental setup considered in this study and a properly selected luminance threshold.

As a matter of fact, the raw images (before applying the differential method) for both algorithms (Figure 12) show similar information and even similar shapes for the high-luminance areas, and therefore this above-mentioned higher robustness of DMAS to the luminance threshold seem to come from the differential stage. It should be noted that DMAS formulation inherently implies noise filtering, which often means detail loss. DMAS differential images (Figure 13) can provide for a robust tracking of the tool's final end, but the information related to the tumor position is blurred. DAS raw images (Figure 12), however, allow to see the tumor and even the cranium shape in addition to the tool, which would allow for intraoperative tracking of the tumor. This is a highly-desirable feature, and therefore the combination of the information extracted from both algorithms could provide the surgical team with a highly accurate intraoperative navigation and guidance for the approach of the surgical tools to the tumor position,

even when changes in the tumor's position are involved, such as those resulting from the brain-shift effect. It should be noted that this would be made only at the expense of a slightly higher computational cost, with no extra hardware required, since both algorithms would independently process the same measurements. The reported system, combining both algorithms, is thereby proposed as a potential surgical navigation system to robustly address interventions prone to tumor's displacements.